PAPER

Check for updates

Improving the optical properties of magnesium spinel chromites through Ni and Cu substitutions for optoelectronic applications

Souhir Heni,[ab] Sobhi Hcini,[b] Mohamed Lamjed Bouazizi, [ID] *[c] Lamjed HajTaieb,[cd] Abdessalem Dhahri[a] and Habib ben Bacha[b]

In this study, we investigated the optoelectronic performance of magnesium spinel chromites with nickel (Ni) and copper (Cu) substitutions. Using the sol–gel method, we synthesized two spinel chromites: $Mg_{0.6}Ni_{0.4}Cr_2O_4$ (MNCO) and $Mg_{0.6}Cu_{0.4}Cr_2O_4$ (MCCO). We extensively characterized these samples to analyze their thermal, structural, elastic, and optical properties. Structural analysis reveals good agreement between the calculated and refined structural parameters, which supports the proposed cation distributions for the samples. By calculating stiffness constants from force constants, we derived elastic moduli such as bulk modulus, longitudinal modulus, and rigidity modulus. MCCO exhibited lower values for these moduli, as well as the Debye temperature, compared to MNCO. Both samples displayed a brittle mechanical nature according to the Pugh ratio, while the Poisson ratio remained constant at 0.25, indicating isotropic elasticity. UV-vis-NIR spectroscopy revealed that MNCO has higher band-gap (E_g) and Urbach (E_u) energies than MCCO. Further analysis of refractive index, penetration depth, extinction coefficients, nonlinear optical parameters, optical conductivity, and optical dielectric constants highlighted the promising optoelectronic applications of the synthesized materials. Our study found that the band-gap energy values of the as-synthesized samples were smaller than reported values for $MgCr_2O_4$ spinel chromites, indicating that Ni and Cu substitutions offer an opportunity to extend the sunlight absorption range of magnesium chromites.

1. Introduction

Spinel ACr_2O_4 chromites (where A represents Fe, Mn, Co, Ni, Cu, and Zn) have garnered considerable attention in research due to their captivating physicochemical properties. These materials have been extensively explored for industrial and technological applications, as evidenced by numerous studies (see ref. 1–3 and references cited therein). Spinel chromites have found utility in a wide range of areas, including solid oxide fuel cells, supercapacitor electrodes, pigments, gas sensors, photo-catalysts, non-volatile memory, and magnetic switching. They exhibit great potential as candidates for nano-device fabrication, sensor components, strengthening agents, combustion catalysts, and protective coatings. Moreover, chromite

nanoparticles have exhibited promise in areas such as photo-catalysis, organic transformation, and superconductivity. Given their diverse applications, spinel ACr_2O_4 chromites play a pivotal role in advancing various scientific and technological fields.

The sol–gel method is a significant approach employed for the production of pure spinel chromites with precise control over their chemical composition and grain size.[1,4] This technique offers numerous advantages, including reduced calcination times, lower processing temperatures, improved material homogeneity, and high purity of the synthesized materials. By adjusting various parameters such as the pH of the initial solution, concentration, calcination time, and calcination temperature, the sol–gel synthesis can further enhance the properties of spinel chromites.[4,5]

As a member of the spinel chromites, magnesium chromium oxides ($MgCr_2O_4$) hold significant importance and offer a wide range of applications due to their exceptional properties (see ref. 6–8 and references therein). $MgCr_2O_4$ chromites exhibit outstanding resistance to thermal shock and demonstrate superior catalytic activity. With a high melting point, they ensure thermal stability even under harsh conditions. Additionally, $MgCr_2O_4$ spinels showcase remarkable mechanical strength at elevated temperatures and possess humidity-

Laboratory of Physical Chemistry of Materials, Physics Department, Faculty of Sciences of Monastir, Monastir University, 5019 Monastir, Tunisia. E-mail: my. bouazizi@psau.edu.sa

Laboratory of Advanced Multifunctional Materials and Technological Applications, Faculty of Science and Technology of Sidi Bouzid, University Campus Agricultural City, University of Kairouan, Sidi Bouzid 9100, Tunisia

Department of Mechanical Engineering, College of Engineering, Prince Sattam bin Abdulaziz University, Alkharj 16273, Saudi Arabia

Laboratory of Applied Fluid Mechanics, Processes Engineering and Environment, National Engineering School of Sfax, University of Sfax, Tunisia

sensing properties. These characteristics make $MgCr_2O_4$ highly desirable in the field of refractory materials, where its stability at high temperatures and resistance to slag attack have been extensively explored.

In terms of optoelectronic properties, $MgCr_2O_4$ spinel chromites have been identified to possess relatively high bandgap energies,[8-10] making them particularly suitable for photodetector applications. The bandgap energies of $MgCr_2O_4$ are close to those observed in some semiconductors such as TiO_2, ZnO, and CuO, which are known for their ability to absorb ultraviolet photons.[11-13] Consequently, due to the higher band gap energies of $MgCr_2O_4$ chromites, they mainly absorb UV photons. While solar light predominantly consists of a minimal proportion of UV photons, accounting for approximately 5% of the total light energy, room-light lamps primarily emit visible photons.[4] In order to expand the spectral response of $MgCr_2O_4$ chromites to include visible light, it is necessary to decrease their band gap energies. In fact, the smaller band gap indicates the higher absorption of visible light in photocatalytic reactions.[4] The purpose of this study is to investigate the optical properties of $MgCr_2O_4$ chromites through the substitution of Ni and Cu. We have employed the sol–gel method to synthesize both $Mg_{0.6}Ni_{0.4}Cr_2O_4$ (MNCO) and $Mg_{0.6}Cu_{0.4}Cr_2O_4$ (MCCO) spinel chromites and investigated their thermal, structural, elastic, and optical properties. The substitution of Ni^{2+} and Cu^{2+} at the tetrahedral (A) site in $MgCr_2O_4$ chromites leads to modifications in their average A-site radius and crystal geometry, which in turn leads to a change in their optical properties. This study reveals significant results for the as-prepared samples. Significantly, the MNCO and MCCO samples demonstrated lower bandgap energies compared to $MgCr_2O_4$ chromites. This suggests the potential for improved visible light absorption of $MgCr_2O_4$ chromites through the substitution of Ni^{2+} and Cu^{2+}. This could be useful in optoelectronic applications, particularly in light-emitting diodes (LEDs). Moreover, the as-synthetized samples possess additional advantages such as their excellent transparency, efficient light absorption, suitability for nonlinear applications, and, above all, their ease and cost-effectiveness of synthesis.

2. Experimental details

The spinel chromites, $Mg_{0.6}Ni_{0.4}Cr_2O_4$ and $Mg_{0.6}Cu_{0.4}Cr_2O_4$, were synthesized via the sol–gel method using high-purity nitrates ($[Mg(NO_3)_2 \cdot 6H_2O]$, $[Cu(NO_3)_2 \cdot 6H_2O]$, $[Ni(NO_3)_2 \cdot 6H_2O]$, and $[Cr(NO_3)_3 \cdot 9H_2O]$). The weighed precursors of each compound were dissolved in distilled water under magnetic stirring on two hot plates at 90 °C, resulting in aqueous solutions. Once the nitrates were completely dissolved, precise amounts of citric acid ($C_6H_8O_7$) were added to each solution as a complexing agent and dissolved under magnetic stirring. Ammonia (NH_4OH) was then added to adjust the pH to approximately 7. Controlled amounts of ethylene glycol ($C_2H_6O_2$) were subsequently added as a polymerization agent. The mixture was continuously heated and stirred until it formed a gel. The obtained gel was dried at 250 °C for 12 hours to achieve a dry foam, which was ground using an agate mortar. To decompose the organic matter, the resulting powders were

annealed at 500 °C for 12 h in an electrical muffle furnace, followed by slow cooling to room temperature. The prepared powders underwent repeated cycles of grinding, pelletizing, and calcination within the temperature range of 600 °C to 1000 °C to promote grain crystallization of the samples, ensuring the formation of single-phase products. In this study, all characterizations were performed on the MNCO and MCCO chromites that were annealed at 1000 °C for 24 h.

The thermal characteristics of the samples were assessed through thermogravimetric analysis (TGA), which was conducted at temperatures ranging from 25 °C to 1000 °C with a temperature step of 0.33 °C. X-ray diffraction (XRD) patterns were obtained using a Panalytical X'Pert Pro System employing Cu-K$_\alpha$ radiation ($\lambda = 1.5406$ Å). The XRD data was collected within an angular range of 10° to 90° with an angular step of 0.02°. Fourier transform infrared (FTIR) spectra were acquired using an FTIR-8400S spectrometer, covering the wavenumber range of 400 cm^{-1} to 1000 cm^{-1} with a step of 1 cm^{-1}. Optical properties were determined at room temperature using a UV-3101PC scanning spectrophotometer. This instrument was equipped with a dual-beam monochromator capable of covering a wavelength spectra from 200 nm to 2400 nm with a wavelength step of 2 nm. Two light sources were utilized for the optical measurements: a xenon lamp for the UV-visible range and a halogen lamp for the infrared range. This technique allows for the determination of absorbance (A) and reflectance (R) as functions of the wavelength. From these two measured optical parameters, the variations of other derived parameters can be studied, such as the absorption coefficient, penetration depth, extinction coefficient, refractive index, and non-linear optical parameters.

3. Results and discussions

3.1. Thermal analysis

The weight losses (W%) for $Mg_{0.6}Ni_{0.4}Cr_2O_4$ and $Mg_{0.6}Cu_{0.4}Cr_2O_4$ samples are shown in Fig. 1. The DTA curves versus
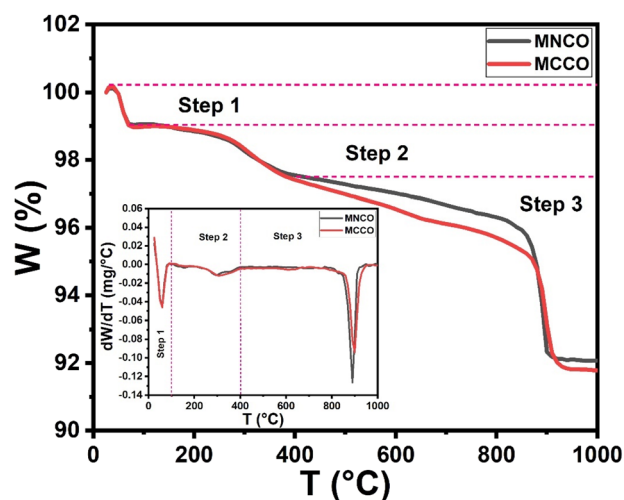

Fig. 1 Thermogravimetric curve (TGA) for MNCO and MCCO spinel chromites. The inset shows the differential thermal curves (DTA).

temperature, also known as differential thermal analysis or the first derivative of weight loss, dW/dT, are also shown in the inset of Fig. 1. It is evident that losing weight primarily involves three steps. A peak in the dW/dT curves centered at 60 °C represents a weight loss that occurs in the first stage, which is ∼1% in the temperature range below 150 °C. The release of water molecules that are lost from beginning hydrated precursors may be indicated by this range of mass loss.[8] The DTA curves for MNCO and MCCO show exothermic peaks at approximately 295 °C and 305 °C, respectively, which occur in the temperature range of 150 °C to 400 °C, which correspond to the second step weight loss and have a maximum weight loss of approximately 1.5%. Within this temperature range, there appears to be a mass decrease that indicates moisture, and leftover gases are escaping.[4] A weight loss of up to 6% occurs during the third stage, which occurs in the 400–1000 °C temperature range. The formation of the spinel phases is indicated by the detection of exothermic peaks in the DTA curves at 890 °C for MNCO and 900 °C for MCCO. As such, it is possible to optimize the calcination temperature to any temperature above 900 °C.

3.2. Structural properties

3.2.1. Theoretical structural analysis. According to earlier research, Mg^{2+}, Ni^{2+}, and Cu^{2+} ions are dispersed throughout the A sites of spinel chromites containing Mg, Ni, Cu, and Cr, whereas Cr^{3+} ions are located at the B sites.[14,15] Thus, (Mg$_{0.6}^{2+}$Ni$_{0.4}^{2+}$)$_A$[Cr$_2^{3+}$]$_B$O$_4^{2-}$ and (Mg$_{0.6}^{2+}$Cu$_{0.4}^{2+}$)$_A$[Cr$_2^{3+}$]$_B$O$_4^{2-}$ can be proposed as the cation distributions for Mg$_{0.6}$Ni$_{0.4}$Cr$_2$O$_4$ and Mg$_{0.6}$Cu$_{0.4}$Cr$_2$O$_4$, respectively. Based on these distributions, we can deduce that the degree of inversion for both samples is equal to zero. Therefore, MNCO and MCCO possess normal spinel structures. The theoretical lattice constant (a_{th}) is calculated using the proposed cation distributions of the MNCO and MCCO samples as follows:[16]

$$a_{th} = \frac{8}{3\sqrt{3}}\left[(r_{tet} + r_O) + \sqrt{3}\,(r_{oct} + r_O)\right] \tag{1}$$

where $r_{tet} = \sum_i C_i r_i$ and $r_{oct} = \frac{1}{2}\sum_i C_i r_i$ are the average ionic radii per molecule for the corresponding A and B-sites; in this case, C_i is the concentration of the element i with ionic radius r_i on a specific site. The ionic radius of oxygen is represented by r_O = 1.38 Å. Table 1 displays the calculated values of a_{th} for MCCO and MNCO. The larger a_{th} value of MCCO compared to MNCO is attributed to the higher ionic radius of Cu^{2+} (0.57 Å) compared to Ni^{2+} (0.55 Å).[17] Using the theoretical lattice constant, the value of the oxygen positional parameter "u" can be calculated as follows:[18]

Table 1 Calculated and refined structural parameters for MNCO and MCCO spinel chromites

Sample		MNCO		MCCO	
Structural parameters		Calculated values	Refined values	Calculated values	Refined values
a (Å)		8.310	8.326 (3)	8.322	8.327 (7)
V (Å^3)		573.856	577.323	576.345	577.468
u		0.3849	0.3846	0.3853	0.3852
δ		0.0099	0.0099	0.0103	0.0103
L_A (Å)		3.5983	3.603	3.6035	3.617
L_B (Å)		2.9380	2.933	2.9423	2.952
d_{AL} (Å)		1.9420	1.941 (4)	1.9500	1.946 (4)
d_{BL} (Å)		1.9884	1.989 (4)	1.9986	1.992 (4)
d_{AE} (Å)		3.1713	3.176 (6)	3.1843	3.179 (6)
d_{BE} (Å)		2.7048	2.704 (6)	2.7002	2.701 (6)
d_{BEU} (Å)		2.9427	2.946 (6)	2.9473	2.948 (6)
Me–Me distances (Å)	b	2.9380	2.935	2.9423	2.942
	c	3.4451	3.454	3.4501	3.461
	d	3.5983	3.602	3.6035	3.608
	e	5.3975	5.401	5.4053	5.432
	f	5.0888	5.087	5.0962	5.094
Me–O distances (Å)	p	1.9950	1.997 (4)	1.9950	1.999 (4)
	q	1.9420	1.946 (4)	1.9500	1.949 (4)
	r	3.7187	3.689 (4)	3.7340	3.695 (4)
	s	3.6495	3.653 (4)	3.6529	3.661 (4)
Bond angles (°)	θ_1	122.098	121.30 (2)	121.990	120.91 (2)
	θ_2	139.750	140.65 (1)	139.300	140.36 (1)
	θ_3	94.840	94.88 (2)	95.028	95.18 (2)
	θ_4	126.35	126.17 (1)	126.39	126.27 (1)
	θ_5	71.212	72.58 (1)	71.923	72.73 (1)
Agreement factors	R_p (%)		5.98		6.66
	R_{wp} (%)		8.12		8.98
	R_{exp} (%)		7.42		7.54
	R_{Bragg} (%)		2.38		3.63
	χ^2 (%)		1.10		1.19

$$u = \left[\frac{1}{\sqrt{3}a}(r_{tet} + r_O) + \frac{1}{4} \right] \quad (2)$$

Table 1 displays the u values of MCCO and MNCO. As observed in this table, the u value remains nearly constant for both samples. In a cubic spinel structure, the ideal u value is 0.375. However, the calculated u values are slightly larger than the ideal value, indicating a possible displacement of the oxygen anion from its ideal position. By analyzing the deviation from the ideal oxygen parameter ($\delta = u - 0.375$), it is confirmed that there is a slight distortion in the lattice for both samples. On the other hand, the inter-ionic distances between magnetic ions, known as the hopping lengths (L_A and L_B), provide insight into the strength of spin interaction between ions in the tetrahedral and octahedral sites. To determine these hopping lengths, Stanley's equations were employed:[18]

$$L_A = \frac{a\sqrt{3}}{4}, \quad L_B = \frac{a\sqrt{2}}{4} \quad (3)$$

Table 1 presents the calculated values of L_A and L_B for both samples. The hopping lengths are higher for MCCO than MNCO. The following equations are provided for the calculation of A and B bond lengths (d_{AL} and d_{BL}), the tetrahedral edge length (d_{AE}), and the shared (d_{BE}) and unshared (d_{BEU}) octahedral edge lengths.[18] These distances are calculated for MNCO and MCCO using the values of a_{th} and u as follows:

$$d_{AL} = a\sqrt{3}\left(u - \frac{1}{4}\right) \quad (4)$$

$$d_{BL} = a\sqrt{3u^2 - \frac{11}{4}u + \frac{43}{64}} \quad (5)$$

$$d_{AE} = a\sqrt{2}\left(2u - \frac{1}{2}\right) \quad (6)$$

$$d_{BE} = a\sqrt{2}(1 - 2u) \quad (7)$$

$$d_{BEU} = a\sqrt{4u^2 - 3u + \frac{11}{16}} \quad (8)$$

Table 1 lists the values for d_{AL}, d_{BL}, d_{AE}, d_{BE}, and d_{BEU} distances for both samples. It is evident from the table that these parameters are higher for MCCO compared to MNCO. Additionally, the cation–anion bond distances (p, q, r, and s) and cation–cation bond distances (b, c, d, e, and f) in spinels (see Fig. 2a) were used to determine the bond angles (θ_1, θ_2, θ_3, θ_4, and θ_5).[19] In spinel materials, metal cations occupy positions A and B, with neighboring cations being their closest neighbors. Consequently, three types of super-exchange interactions exist: A–A, B–B, and A–B. These interactions can be further categorized into five types due to variations in the chemical bond angles between metal cations and oxygen ions. The bond angles θ_1 and θ_2 correspond to A–O–B interactions, θ_3 and θ_4 relate to B–O–B interactions, and θ_5 is associated with A–O–A

interactions. Fig. 2a illustrates the configuration of ion pairs in spinel materials with favorable distances. By applying the principle of super-exchange and considering the five relative positions in Fig. 2a, it becomes evident that A–B super-exchange is the strongest, followed by B–B super-exchange, while A–A super-exchange is the weakest. The following equations were used to calculate the cation–anion (Me–O) distances, cation–cation (Me–Me) distances, as well as the bond angles (Me–O–Me):[18,19]

$$b = \frac{a\sqrt{2}}{4}, \quad c = \frac{a\sqrt{11}}{8}, \quad d = \frac{a\sqrt{3}}{4}, \quad e = \frac{3\sqrt{3}a}{8}, \quad f = \frac{a\sqrt{6}}{4} \quad (9)$$

$$p = a\left(\frac{5}{8} - u\right), \quad q = a\sqrt{3}\left(u - \frac{1}{4}\right), \quad r = a\sqrt{11}\left(u - \frac{1}{4}\right), \quad s = a\sqrt{3}\left(\frac{u}{3} + \frac{1}{8}\right) \quad (10)$$

$$\theta_1 = \cos^{-1}\left(\frac{p^2 + q^2 - c^2}{2pq}\right) \quad (11)$$

$$\theta_2 = \cos^{-1}\left(\frac{p^2 + r^2 - e^2}{2pr}\right) \quad (12)$$

$$\theta_3 = \cos^{-1}\left(\frac{2p^2 - b^2}{2p^2}\right) \quad (13)$$

$$\theta_4 = \cos^{-1}\left(\frac{p^2 + s^2 - f^2}{2ps}\right) \quad (14)$$

$$\theta_5 = \cos^{-1}\left(\frac{r^2 + q^2 - d^2}{2qr}\right) \quad (15)$$

The calculated values of all these parameters are displayed in Table 1. The table clearly demonstrates that the Me–Me and Me–O distances are higher for MCCO compared to MNCO. In addition, the analysis of the data presented in Table 1 reveals the dominance of A–B interactions over A–A and B–B interactions, corroborating the findings depicted in Fig. 2a. Moreover, the bond angles exhibit a trend that alternates between decreasing and increasing for both MCCO and MNCO samples.

3.2.2. Rietveld refinement of experimental XRD patterns.

The crystalline structure and phase purity of the $Mg_{0.6}Ni_{0.4}Cr_2O_4$ and $Mg_{0.6}Cu_{0.4}Cr_2O_4$ samples were confirmed by XRD analysis, as illustrated in Fig. 2b. The diffraction peaks show cubic spinel phases for both samples according to the space group $Fd\bar{3}m$. Furthermore, the XRD patterns verify that the produced powders are homogeneously crystallized, displaying a single, pure phase devoid of any other phases. The positions and intensities of all distinguishable peaks closely corresponded to those found in the standard JCPDS card no. 77-0007.[8] Furthermore, the XRD patterns exhibit a slight shift towards lower diffraction angles for MCCO compared to MNCO, as observed in the inset of Fig. 2b. This shift indicates a higher lattice constant (a) and cell volume (V) for MCCO. The experimental analysis of the synthesized samples involved the utilization of Rietveld refinement,[20] employing the proposed cation
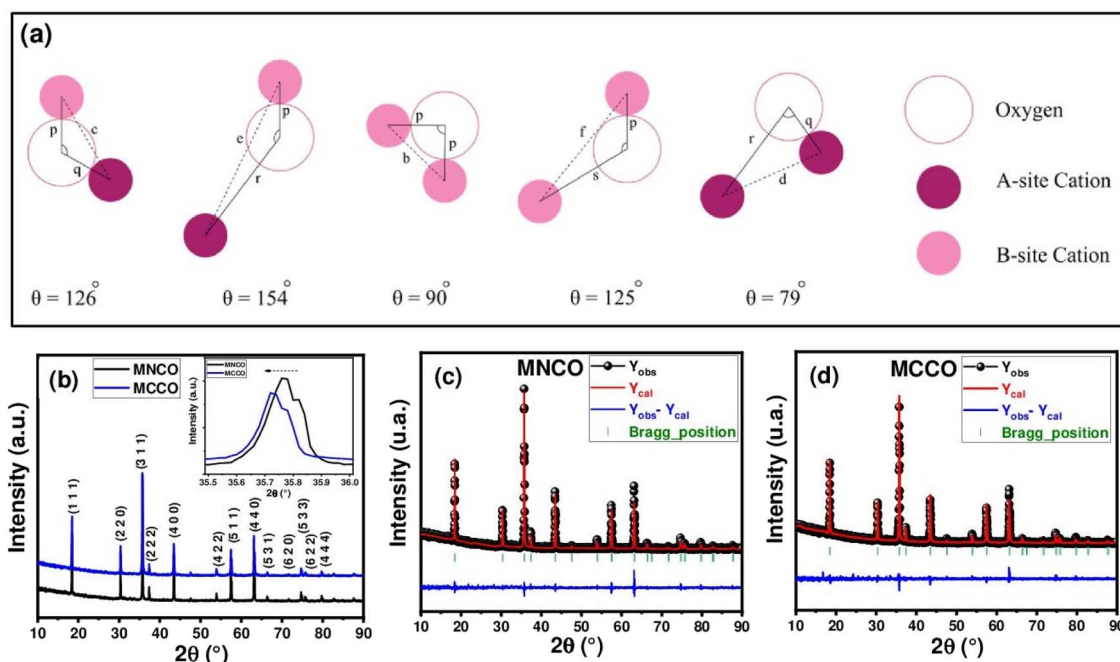
Fig. 2 (a) Favorable interionic distances and angles in spinel samples for better magnetic interaction. (b) XRD patterns for MNCO and MCCO spinel chromites. All peaks are indexed in the cubic spinel type structure ($Fd\bar{3}m$ space group). The inset shows observed XRD profiles of the most intense peaks (Bragg reflections (3 1 1)). (c and d) Structural refinement of the XRD patterns using Rietveld method for MNCO and MCCO, respectively.

distributions discussed in Section 3.2.1. The difference between the calculated and observed patterns is illustrated in Fig. 2(c) and (d). The Rietveld refinement assigned B cations, A cations, and oxygen to positions 16d (1/2, 1/2, 1/2), 8a (1/8, 1/8, 1/8), and 32e (x, y, z), respectively. The reliability of the Rietveld fitting was evaluated using the R-factors (expected R_{exp}, Bragg R_{Bragg}, profile R_p, and weighted profile R_{wp}), all of which were found to be less than 10%. The goodness of fit, represented by $\chi^2 = R_{wp}/R_{exp}$, was close to one, indicating a good fit. The atomic position of oxygen (0.2618(4) for MNCO and 0.2625(4) for MCCO) adheres to the spinel's typical characteristics. Table 1 summarizes the refined structural parameters and compares them to the theoretical values from Section 3.2.1. The good agreement between the refined and calculated structural parameters supports the proposed cation distribution for the $Mg_{0.6}Ni_{0.4}Cr_2O_4$ and $Mg_{0.6}Cu_{0.4}Cr_2O_4$ chromite samples. Based on the data presented in Table 1, it is evident that the refined lattice constants of our samples are higher in comparison to the undoped $MgCr_2O_4$ chromites.[6,9] This increase can be attributed to the difference in the ionic radii between Ni^{2+}, Cu^{2+}, and Mg^{2+}.[17] Furthermore, we calculated the average crystallite size (D) using the Debye–Scherrer formula.[6] The average crystallite size for MCCO (104 nm) is greater than that of MNCO (98 nm). This discrepancy can be attributed to the larger ionic radius of Cu^{2+} in comparison to Ni^{2+}. Additionally, we determined the experimental X-ray density (ρ_x)[6] for both samples. The difference in density values between MNCO (4.74 g cm^{-3}) and MCCO (4.78 g cm^{-3}) can be attributed to the fact that nickel has a lower density (8.91 g cm^{-3}) compared to copper (8.96 g cm^{-3}).[21]

3.3. Infrared and elastic properties

3.3.1. FTIR spectra analysis. The FTIR spectra were analyzed to investigate the functional groups present in the samples and to determine the vibrational frequencies of the network structures. Fig. 3a displays the infrared spectra of MCCO and MNCO chromite spinels. These spectra exhibit two absorption bands related to the vibrational bands of incorporated metal oxides.[1,9,10] The presence of these bands confirms the successful synthesis of the chromite samples with metal-oxide bonds involving Ni, Cu–O and Cr–O. The first band (ν_B), observed near 450 cm^{-1}, is attributed to metal–oxygen (Cr–O) stretching vibrations at the octahedral site. The second band (ν_A), appearing near 560 cm^{-1}, is associated with the generation of tetrahedral bonds (Ni, Cu–O). Upon examining Fig. 3a, it becomes evident that the bands associated with metal–oxygen stretching vibrations at both the octahedral and tetrahedral sites demonstrate a slight shift towards lower wavenumbers in the case of MCCO when compared to MNCO. As presented in Table 2, the ν_A value decreases from 575 cm^{-1} for MNCO to 566 cm^{-1} for MCCO. However, the ν_B value decreases from 461 cm^{-1} for MNCO to 455 cm^{-1} for MCCO. This decrease in the bands associated with metal–oxygen stretching vibrations at both the A and B sites can indeed be related to the higher Me–O distances for MCCO compared to MNCO, as shown in the structural part. In spinel structures, the vibrational frequencies of metal–oxygen stretching vibrations are influenced by the bond lengths and bond strengths. When the cation–oxygen bond length increases, it indicates a lengthening of the bonds between the metal cations and oxygen atoms. The elongation of the cation–oxygen bond
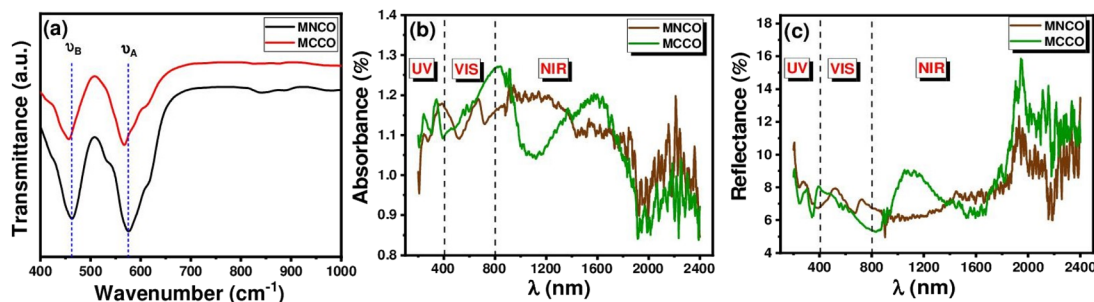
Fig. 3 (a) FTIR spectra for MNCO and MCCO spinel chromites. (b) UV-vis-NIR absorbance spectra *versus* wavelength. (c) Reflectance spectrum $R(\lambda)$.

lengths leads to a decrease in bond strength, which in turn results in a decrease in the vibrational energy of the metal–oxygen bonds. This decrease is reflected in the FTIR spectra as a shift towards lower wavenumbers or frequencies for the bands associated with metal–oxygen stretching vibrations. Therefore, as the Me–O distances are higher for MCCO compared to MNCO, the metal–oxygen stretching vibrations at both sites experience a decrease in vibrational energy. This decrease is manifested as a shift towards lower wavenumbers in the FTIR spectra.

3.3.2. Elastic properties. Spinel materials exhibit significant elastic and thermal properties due to the existence of interatomic and interionic forces. The most popular technique for figuring out elastic constants and Debye temperatures is ultrasonic pulse transmission.[22] Even though the elastic properties of these materials are governed by external stresses, several studies have examined the correlations between elastic, thermal, structural, and infrared properties. Modi *et al.* developed a detailed method for investigating the elastic properties of spinel systems using FTIR spectra.[23] The force constants (K_t) for the tetrahedral site and (K_o) for the octahedral site are directly related to the active infrared phonon mode's wavenumbers ν_A and ν_B. The following

Waldron relations were used to calculate the force constants (K_t) and (K_o) in the cubic spinel structure:[16]

$$K_t = 7.62 \times M_A \times \nu_A^2 \times 10^{-7}, \quad K_o = 10.62 \times \left(\frac{M_B}{2}\right) \times \nu_B^2 \times 10^{-7}$$

(16)

The molecular mass M_A at the A sites was calculated using the molecular masses of Mg, Ni and Cu elements as $M_A = 0.6 \times M(Mg) + 0.4 \times M(Ni) = 38.06$ g mol^{-1} for $(Mg_{0.6}^{2+}Ni_{0.4}^{2+})_A[Cr_2^{3+}]_BO_4^{2-}$ and $M_A = 0.6 \times M(Mg) + 0.4 \times M(Cu) = 40.00$ g mol^{-1} for $(Mg_{0.6}^{2+}Cu_{0.4}^{2+})_A[Cr_2^{3+}]_BO_4^{2-}$. However, the molecular mass (M_B) at the B sites remained constant for both samples, with a value of $M_B = 2 \times M(Cr) = 103.99$ g mol^{-1}. Table 2 presents the comparison between the force constants (K_t and K_o) and the average force constant $\left(K_{av} = \frac{K_t + K_o}{2}\right)$ for MNCO and MCCO samples. It is evident that the estimated K_o values are significantly higher than the corresponding K_t values for both samples. Additionally, the average force constant K_{av} is lower for MCCO in comparison to MNCO. This decrease in K_{av} is typically associated with the longer Me–O bond distances observed in MCCO compared to MNCO. Hook's law establishes a relationship between stress (σ_i), strain (ε_{ij}), and stiffness (C_{ij}) through the stress–strain approach.[23] The stiffness values (C_{ij}) play a crucial role in determining the elastic constants. In the case of cubic symmetry, only three dominant stiffness values are considered: C_{11}, C_{12}, and C_{44}. Among these, C_{11} represents elasticity in length, while C_{12} and C_{44} represent elasticity in shape. The stiffness coefficients (C_{11}, C_{12}, and C_{44}) were calculated using the following equations:[18]

$$C_{11} = \frac{k_{av}}{a}, \quad C_{12} = \frac{\sigma \, C_{11}}{1 - \sigma}, \quad C_{44} = \rho^2 \nu_t \tag{17}$$

In these equations, a represents the unit cell parameter, ρ represents the X-ray density, $\nu_t = \frac{\nu_l}{\sqrt{3}}$ is the transverse wave velocity (where $\nu_l = \sqrt{\frac{C_{11}}{\rho}}$ is the longitudinal wave velocity), and $\sigma = \frac{L - 2G}{2(L - G)}$ is the Poisson's ratio (where $L = \rho\nu_l^2$ and $G = \rho\nu_t^2$

Table 2 Elastic and thermal parameters for MNCO and MCCO spinel chromites

Sample		MNCO	MCCO
Absorption bands (cm^{-1})	ν_B	461	455
	ν_A	575	566
Force constant (N m^{-1})	K_t	95.89	97.65
	K_o	117.35	114.32
	K_{av}	106.62	105.98
Stiffness constant (GPa)	C_{11}	128.05	127.27
	C_{12}	42.68	42.42
	C_{44}	67.42	68.07
Wave velocity (m s^{-1})	ν_l	5197.51	5160.01
	ν_t	3000.78	2979.13
	ν_m	3331.44	3307.40
Longitudinal modulus (GPa)	L	128.05	127.27
Rigidity modulus (GPa)	G	42.82	42.42
Bulk modulus (GPa)	B	71.14	70.71
Poisson's ratio	σ	0.25	0.25
Pugh ratio	B/G	1.661	1.667
Debye temperature (K)	θ_D	455.96	452.53
Thermal conductivity (W m^{-1} K^{-1})	K_{min}	0.97	0.96

indicate the longitudinal and rigidity moduli, respectively). The values of stiffness constants, transverse and longitudinal wave velocity, rigidity and longitudinal moduli, and Poisson's ratio are all tabulated in Table 2. The lower values of ν_l and ν_t for MCCO than MNCO may be ascribed to the decrease of average force constant K_{av}. For both samples, the Poisson ratio remains constant at $\sigma = 0.25$. This value is consistent with the isotropic elasticity theory because it falls between -1 and 0.5.[18] Furthermore, it is noted from Table 2 that the stiffness constants (C_{11} and C_{12}) are lower for MCCO than MNCO. Besides, to ascertain the ductility or brittleness of the prepared materials based on the Pugh criteria,[18] the ratio between the bulk modulus ($B = 1/3(C_{11} + 2C_{12})$) and the rigidity modulus (G) was evaluated. A ductile material's B/G ratio should be greater than 1.75, whereas a brittle material should be smaller than 1.75. Table 2 demonstrates that MCCO exhibits lower values for the bulk modulus (B), rigidity modulus (G), and longitudinal modulus (L) compared to MNCO. The change in these elastic moduli for both MNCO and MCCO can be attributed to the interatomic binding between different atoms within their spinel lattices. In addition, the calculated values of the Pugh ratio are below the critical value of 1.75, suggesting the brittle mechanical nature of the prepared samples. On the contrary, the Debye temperature (θ_D) is an essential parameter that characterizes the upper limit of atomic lattice vibrations and provides valuable insights into the thermodynamic properties of a solid. The following equation can be used to estimate the θ_D value in accordance with Anderson's formula:[23]

$$\theta_D = \frac{\hbar}{k_B}\left(\frac{3q\rho N_A}{4\pi M}\right)^{\frac{1}{3}}\nu_m \quad (18)$$

where k_B is Boltzmann's constant, $\hbar$ is Planck's constant, M is the molecular mass, ρ is the X-ray density, N_A is Avogadro's number, q is the number of atoms per unit formula (equals to 7 in a cubic spinel system), and $\nu_m = \left(\frac{1}{3}\left(\frac{2}{\nu_t^3} + \frac{1}{\nu_l^3}\right)\right)^{-1/3}$ represents the mean wave velocity. In addition, the thermal conductivity is a thermodynamic property that quantifies a material's capacity to conduct heat. The minimum value of thermal conductivity, represented as K_{min}, can be determined using this equation:[18]

$$K_{min} = \left(\frac{M}{q\rho N_A}\right)^{-\frac{2}{3}}k_B\nu_m \quad (19)$$

In Table 2, it is observed that the calculated values of θ_D, ν_m, and K_{min} are consistently lower for MCCO compared to MNCO. The decrease in ν_m can be attributed to the lower transverse and longitudinal wave velocities (ν_l and ν_t) observed in MCCO. Furthermore, the lower Debye temperature for MCCO can be attributed to the reduced bonding strength in this sample.[24]

3.4. Optoelectronic properties

3.4.1. UV-vis-NIR absorbance and reflectance spectra. Fig. 3(b) and (c) shows the reflectance spectra ($R(\lambda)$) and absorption spectra ($A(\lambda)$) of $Mg_{0.6}Ni_{0.4}Cr_2O_4$ and $Mg_{0.6}Cu_{0.4}Cr_2O_4$ chromites. The $A(\lambda)$ data show UV-vis absorption bands, indicating that the samples are capable of efficiently absorbing UV-vis light. They are therefore attractive options for photocatalysis materials.[25,26] The compounds also show NIR absorption bands, indicating that they could be suitable candidates for NIR optoelectronic devices.[4] For both samples, the band gap energies were estimated using Tauc's law as follows:[5,10]

$$\alpha h\nu = \beta(h\nu - E_g)^n \quad (20)$$

where $\alpha = 2.303 \times A/d$ is the optical absorption coefficient (with A is the absorbance and d is the thickness of each sample), E_g is the band-gap energy, $h\nu$ is the photon energy, and β is a parameter describing the compound's degree of disorder. The value of the exponent n denotes the type of optical transition: direct optical transitions for $n = 1/2$ and indirect optical transitions for $n = 2$. Accordingly, the following equation is employed to validate the optical transition in the samples:

$$\ln(\alpha h\nu) = \ln(\beta) + n\ln(h\nu - E_{gd}) \quad (21)$$

Based on the $[(\alpha h\nu)^{1/2}$ vs. $h\nu]$ curves depicted in Fig. 4(a) and (b), it can be observed that neither of the samples demonstrate indirect optical transitions. From the $[(\alpha h\nu)^2$ vs. $h\nu]$ curves shown in Fig. 4(a) and (b), the direct (E_{gd}) band gap values were determined to be 2.78 eV for MNCO and 2.65 eV for MCCO. The $[\ln(\alpha h\nu)$ vs. $\ln(h\nu - E_g)]$ curves in Fig. 4(c) and (d) indicate that the n exponent values are approximately 0.5 for both samples. Therefore, both MNCO and MCCO spinel chromites exhibit a direct optical transition, consistent with previous findings on other spinel chromites.[4,26] This direct optical transition indicates a direct band gap that allows for the movement of electrons from the valence band to the conduction band without the presence of intermediate energy states. With their remarkable light-absorbing and light-emitting properties, these samples are well-suited for applications in solar cells, lasers, and optoelectronic devices. According to the data in Table 3, the band gap energy (E_g) decreases from 2.78 eV for MNCO to 2.65 eV for MCCO. The band gap energy is typically influenced by factors such as grain size, structural parameters, and impurities.[4] In the structural part, our findings indicate that the grain size is higher in MCCO compared to MNCO. With an increase in grain size, the presence of grain boundaries is reduced. This reduction in grain boundaries leads to a decrease in the scattering of carriers at these boundaries, ultimately resulting in a lower band gap energy (E_g) for MCCO compared to MNCO. Furthermore, the enlargement of grain size can also minimize the effects of quantum confinement, thereby contributing to the overall reduction in the band gap energy. The band gap energies (E_g) of the as-prepared samples, presented in Table 3, have been compared to those of some semiconductors[11–13] and other spinel chromites.[2,3,8–10,25,27–30] It is worth noting that materials with larger E_g values are known to absorb ultraviolet (UV) photons, as evidenced by the values provided for some semiconductors[11–13] in Table 3. However, since sunlight primarily consists of visible light (with only around 5% UV
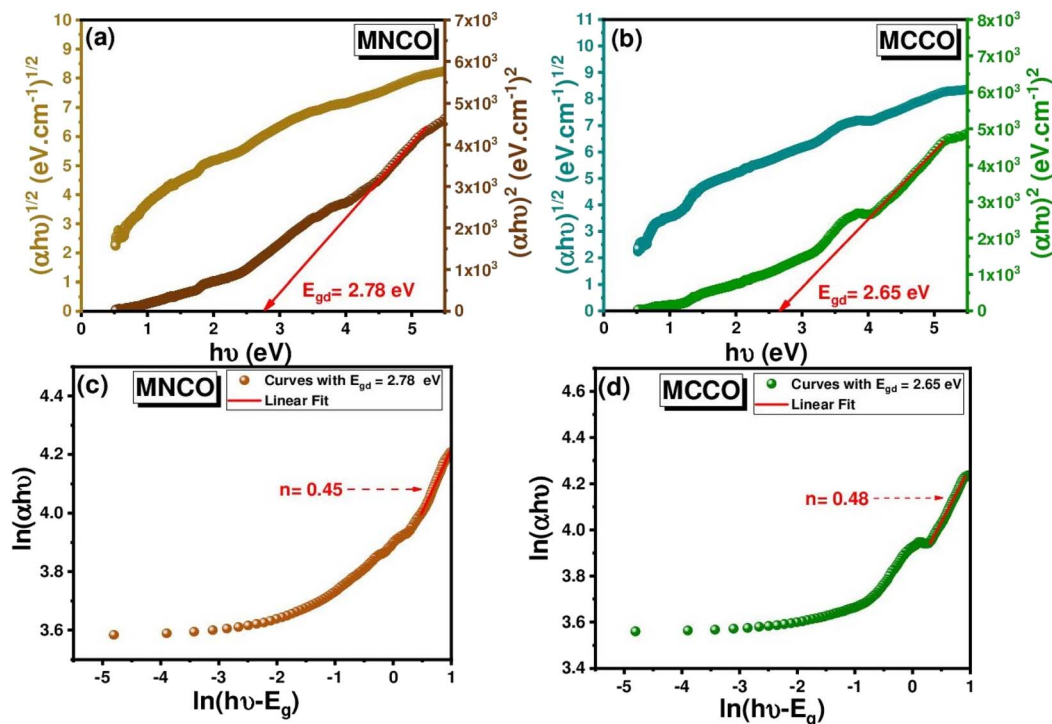
Fig. 4 (a and b) Plots of $(\alpha h\nu)^{1/2}$ and $(\alpha h\nu)^2$ versus $h\nu$ for MNCO and MCCO spinel chromites. (c and d) Plots of $\ln(\alpha h\nu)$ versus $\ln(h\nu - E_g)$.

photons) and most room-light lamps emit visible photons,[4] there is a growing interest in studying materials for their response to visible light.[2,3,25,27] Notably, the estimated E_g values for the as-synthesized MNCO and MCCO samples are lower than those reported for certain semiconductors and other spinel chromites.[11–13,28–30] A lower band gap energy allows for greater absorption of visible light in photocatalytic reactions,[27] making our samples potential candidates for visible light absorption. Additionally, our study revealed that the band gap

Table 3 Band gap energies for MNCO and MCCO spinel chromites compared to those reported in previous works

Sample	Band gap energy (eV)	Reference
TiO_2	3.20	11
ZnO	3.37	12
CuO	3.85	13
$CoCr_2O_4$	1.19	2
$ZnCr_2O_4$	1.80	3
$Ni_{0.5}Mn_{0.5}Cr_2O_4$	1.90	27
$Ni_{0.7}Cd_{0.3}Cr_2O_4$	2.20	25
$CuCr_2O_4$	3.55	28
$Mg_{0.5}Zn_{0.5}Cr_2O_4$	3.46	29
$Mg_{0.5}Zn_{0.3}Co_{0.2}Cr_2O_4$	3.00	29
$CdCr_2O_4$	3.5	30
$Cd_{0.5}Co_{0.5}Cr_2O_4$	3.325	30
$CoCr_2O_4$	3.00	30
$MgCr_2O_4$	3.10	8
$MgCr_2O_4$	3.47	9
$MgCr_2O_4$	2.98	10
$Mg_{0.6}Ni_{0.4}Cr_2O_4$	2.78	This work
$Mg_{0.6}Cu_{0.4}Cr_2O_4$	2.65	This work

energy values of the synthesized samples were smaller than the reported values for $MgCr_2O_4$ chromites, which are typically employed as photocatalysts under UV illumination.[8–10] This suggests that the substitution of Ni and Cu provides an opportunity to extend the sunlight absorption range of $MgCr_2O_4$ spinel chromites. It is important to note that the E_g values for the MCCO and MNCO samples also exceed the minimum energy requirement for water splitting ($E_g > 1.23$ eV). Consequently, our samples can also serve as photocatalytic materials.[4]

3.4.2. Penetration depth and extinction coefficient. The penetration depth (δ) describes how deeply light or radiation can penetrate a material.[26] It depends on the material's ability to reduce the intensity of incident radiation. The variation of $\delta(\lambda)$ can be estimated using the reciprocal of the absorption coefficient ($\alpha(\lambda)$). The $\delta(\lambda)$ curves for MCCO and MNCO chromite samples in Fig. 5a exhibit distinct variations in relation to the absorption coefficient. In the UV-vis-NIR regions, the $\delta(\lambda)$ curves show specific absorption features with different intensities. Light can penetrate deeper into the materials within these three wavelength ranges. Fig. 5a also shows lower values of $\delta(\lambda)$ for both samples. Similar orders of magnitude in $\delta(\lambda)$ values have been observed for other spinel chromites.[25–27] This indicates improved light absorption and energy conversion efficiency for MCCO and MNCO chromites. They are also suitable for high-performance photodetectors, detecting light across various wavelengths.

The extinction coefficient (k) can be calculated using the product of the absorption coefficient (α) and the wavelength (λ), divided by 4π.[25] Fig. 5b demonstrates the behavior of the k coefficient in relation to photon energy ($h\nu$) for MCCO and

Fig. 5 (a) Penetration depth (δ) *versus* λ and (b) extinction coefficient (k) *versus* $h\nu$ for MNCO and MCCO spinel chromites. (c and d) Plot of $\ln(\alpha)$ *versus* $h\nu$. The insets show the curve of $(\alpha/\lambda)^2$ *vs.* $1/\lambda$.

MNCO samples. Notably, the k-values exhibit higher values at lower $h\nu$ values, but as $h\nu$ increases, they dramatically decrease and approach zero, indicating minimal light loss within the higher energy range. Similar trends in k values decreasing as the photon energy increases have been observed in other materials.[4,27] The change in k values falls within the order of 10^{-4}, indicating that the scattering and absorption losses during light propagation through the samples are minimal. This behavior signifies the good transparency of MCCO and MNCO chromites.

3.4.3. Urbach energy. The Urbach energy (E_u) is a parameter used in optical spectroscopy to characterize the degree of disorder, impurities, and defects in a material.[25] It provides information about the localized states within the band gap and the broadening of electronic transitions. It represents the characteristic decay length of the exponential tail and is inversely proportional to the spatial extent of localized states. A smaller E_u value indicates a more ordered and less disordered material, while a larger E_u value corresponds to a higher density of defects and disorder. The Urbach energy (E_u) can be determined from the photon energy ($h\nu$) as follows:[27]

$$\alpha = \alpha_0 \exp\left(\frac{h\nu}{E_u}\right) \qquad (22)$$

In this equation, α represents the absorption coefficient, and α_0 is a constant. The logarithmic form of this equation is often used to analyze experimental data and extract the Urbach

energy from absorption spectra. In Fig. 5(c) and (d), the Urbach energy (E_u) values (see Table 4) were extracted from the [$\ln(\alpha)$ *vs.* ($h\nu$)] curves. Table 4 indicates that the E_u value decreases from 2.14 eV for MNCO to 1.86 eV for MCCO. These values exceed the Urbach energies obtained at room temperature for certain conventional semiconductor materials like ZnO ($E_u = 0.067$

Table 4 The values of optical parameters for MNCO and MCCO spinel chromites

Sample	MNCO	MCCO
E_g (eV)	2.78	2.65
E_u (eV)	2.14	1.86
S	0.012	0.014
E_{e-ph} (eV)	55.55	47.62
λ_T (nm)	580	487
n_0	1.92	1.64
n_1	0.024	0.010
n_2	0.162	0.355
E_0 (eV)	5.66	4.62
E_d (eV)	17.65	7.22
ε_{op}	4.19	2.56
n_0'	2.03	1.60
λ_0 (nm)	468	455
S_0 (10^{-6} m^{-2})	11.55	6.94
n_0''	1.59	1.19
$\chi^{(1)}$ (SI)	0.224	0.139
$\chi^{(3)}$ (10^{-13} m^2 V^{-2})	4.26	0.64
n_2 (10^{-12} m^2 V^{-1})	8.25	1.45

© 2024 The Author(s). Published by the Royal Society of Chemistry

eV)[31] and GaAs ($E_u = 0.044$ eV).[32] This highlights the significance of disorder and defects in the as-prepared samples when comparing them to these semiconductor materials. However, the estimated E_u values for the MNCO and MCCO spinels are consistent with those reported for other spinel systems, such as $Ni_{0.5}Mn_{0.5}Cr_2O_4$ ($E_u = 2.34$ eV)[27] and $ZnFe_{1.96}Co_{0.04}O_4$ ($E_u = 1.861$ eV).[33] On the other hand, the lower E_u value for MCCO compared to MNCO can be attributed to the larger grain size of MCCO in comparison to MNCO. The decrease in Urbach energy with an increase in grain size can be explained by the reduction in structural disorder and defects within the material. When grain size increases, the material's crystalline structure becomes more continuous and coherent, resulting in fewer structural imperfections such as grain boundaries, dislocations, and defects. The Urbach energy (E_u) can be related to the steepness parameter $S(T)$ through this equation:[34]

$$E_u = \frac{k_B T}{S(T)} \tag{23}$$

In this equation, k_B represents the Boltzmann constant, and T represents the room temperature. The steepness parameter, $S(T)$, describes the broadening of the absorption edge caused by interactions between electrons–phonons or excitons–phonons, as referenced in ref. 35. It quantifies the rate at which the absorption coefficient changes with respect to photon energy near the band edge. A larger $S(T)$ value indicates a steeper absorption edge and a broader energy range over which the absorption coefficient changes significantly. As shown in Table 4, the S parameter was estimated to be 0.012 and 0.014 for MNCO and MCCO, respectively. In this case, the higher $S(T)$ value for MCCO indicates a greater broadening of the absorption edge compared to MNCO. According to eqn (24), the electron–phonon interaction energy (E_{e-ph}) can be estimated from the S parameter as:[35]

$$E_{e-ph} = \frac{2}{3S} \tag{24}$$

The E_{e-ph} value represents the energy associated with the interaction between electrons and phonons in the material. It is an important parameter in understanding the electronic and thermal properties of a material. A higher E_{e-ph} value indicates a stronger electron–phonon interaction, suggesting that the material has a higher propensity for energy dissipation through lattice vibrations. In our case, by applying eqn (24), we have determined the E_{e-ph} values for our samples as 55.55 eV for MNCO and 47.62 eV for MCCO (see Table 4). The higher E_{e-ph} value for the MNCO sample suggests a stronger electron–phonon interaction, indicating a higher propensity for energy dissipation through lattice vibrations compared to the MCCO sample. On the other hand, in optoelectronic devices, the maximum wavelength of incident radiation, denoted as λ_T, also known as the threshold wavelength or critical wavelength, is a significant factor in determining the suitability of a compound for such applications. The λ_T value represents the minimum wavelength of light required to initiate specific optoelectronic processes, such as absorption or emission, in a material. To estimate the λ_T values, we have used this equation:[34]

$$\left(\frac{\alpha}{\lambda}\right)^2 = C\left(\frac{1}{\lambda}\right) - \left(\frac{1}{\lambda_T}\right) \tag{25}$$

where α represents the absorption coefficient, λ is the wavelength of incident radiation, and C is a constant. As mentioned in the insets of Fig. 5(c) and (d) and Table 4, the fitting curves yield values of λ_T that decrease from 580 nm for MNCO to 487 nm for MCCO. The observed decrease in λ_T indicates that the bandgap energy of the MCCO material is lower compared to the MNCO sample, consistent with previous observations. In general, a lower bandgap energy corresponds to a lower threshold wavelength. This implies that the material requires larger-energy photons (lower wavelengths) to initiate optoelectronic processes.

3.4.4. Refractive index. The refractive index (n) is an important parameter in the field of spectral dispersion applications. It characterizes how light propagates through a material and is influenced by factors such as the material's composition, density, and optical properties. The refractive index (n) can be estimated using the $R(\lambda)$ and the $k(\lambda)$ data as follows:[25]

$$n(\lambda) = \frac{1+R}{1-R} - \sqrt{\frac{4R}{(1-R)^2} - (k(\lambda))^2} \tag{26}$$

In Fig. 6(a) and (b), the $n(\lambda)$ curves for the MNCO and MCCO spinel chromites are displayed. The presence of high absorption bands in the UV-vis-NIR zones indicates the high quality and compactness of the samples.[26] To model the variations of the refractive index (n) with wavelength, the following Cauchy relation is used:

$$n = n_0 + \frac{n_1}{\lambda^2} + \frac{n_2}{\lambda^4} \tag{27}$$

In this equation, n_0, n_1 and n_2 represent the Cauchy parameters, which describe the wavelength dependence of the refractive index. The insets of Fig. 6(a) and (b) illustrate the variations of the refractive index (n) $versus$ $\left(\frac{1}{\lambda^2}\right)$, as modeled by eqn (27). The Cauchy parameters were estimated in Table 4 for MNCO and MCCO samples. These Cauchy parameters provide a mathematical representation of how the refractive index (n) varies with wavelength for our samples. They provide valuable information for applications involving spectral dispersion and light propagation in materials.

Dispersion is a crucial factor that plays a significant role in material selection for potential applications and the design of optoelectronic devices with spectral dispersion.[36] Thus, in order to comprehend the dispersion parameters of the refractive index and dispersion energies of $Mg_{0.6}Ni_{0.4}Cr_2O_4$ and $Mg_{0.6}Cu_{0.4}Cr_2O_4$ spinel chromites, a thorough discussion of this topic is required. Wemple–Di-Domenico's Single Effective Oscillator Model[37] is the best model to study these parameters. The
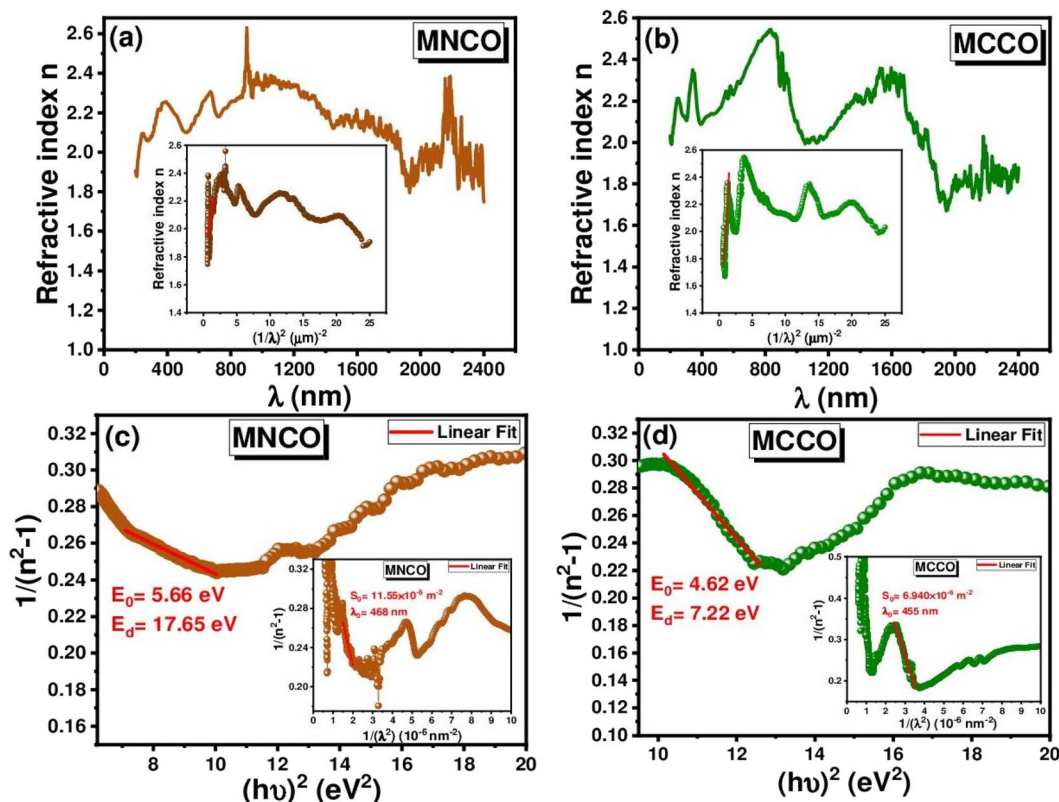
Fig. 6 (a and b) Refractive index n versus λ for MNCO and MCCO spinel chromites, respectively. The insets show the fit of $n(\lambda)$ curves using Cauchy relation. (c and d) Plots of $1/(n^2 - 1)$ versus $(h\nu)^2$ for MNCO and MCCO, respectively. The insets show the plots of $1/(n^2 - 1)$ versus $(1/\lambda^2)$.

effective single oscillator energies (E_0) and dispersion or strength energies (E_d) have been successfully investigated by this model. The refractive index (n) and the energies (E_0 and E_d) are connected by the following expression, per the Wemple and Di-Domenico dispersion theory:[37]

$$n^2 - 1 = \frac{E_0 E_d}{E_0{}^2 - (h\nu)^2} \qquad (28)$$

This equation can be graphically represented by plotting the refractive index factor $[1/(n^2 - 1)]$ against the square of photon energy $[(h\nu)^2]$. Fig. 6(c) and (d) illustrates this graphical representation. By analyzing the resulting straight line, one can determine the slope $[1/(E_0 E_d)]$ and the y-axis intercept (E_0/E_d). Therefore, the energy values of E_0 and E_d can be easily obtained for MNCO and MCCO from Fig. 6(c) and (d) and presented in Table 4. According to Tanaka,[38] E_0 is approximately twice the value of the bandgap energy (E_g). With the estimated values of E_0 and E_d, we can calculate the zero-frequency dielectric constant $\left(\varepsilon_{op} = 1 + \frac{E_d}{E_0}\right)$ and the static refractive index $\left(n_0' = \sqrt{1 + \frac{E_d}{E_0}}\right)$. As presented in Table 4, the calculated values were calculated as $\varepsilon_{op} = 4.19$ and $n_0' = 2.03$ for MNCO and as $\varepsilon_{op} = 2.65$ and $n_0' = 1.60$ for MCCO. It is noteworthy that the calculated values of the static refractive index (n_0') agree well

with the n_0 values estimated from the Cauchy fit. This agreement indicates the consistency and reliability of the results obtained through different methods. The average oscillator strength (S_0) and the oscillator wavelength (λ_0) for the MNCO and MCCO samples were determined using eqn (29).[36] This equation relates the refractive index (n), the average oscillator strength (S_0), the oscillator wavelength (λ_0), and the wavelength (λ) of the light as follows:

$$\frac{1}{n^2 - 1} = \frac{1}{S_0 \lambda_0{}^2} - \frac{1}{S_0 \lambda^2} \qquad (29)$$

As shown in the insets of Fig. 6(c) and (d), the curves of $\left[\left(\frac{1}{n^2 - 1}\right) \ vs. \ \frac{1}{\lambda^2}\right]$ were plotted. From these plots, the values of λ_0 were determined as 468 nm for MNCO and 455 nm for MCCO (see Table 4). The S_0 values were found to be $11.55 \times 10^{-6} \ \text{m}^{-2}$ and $6.94 \times 10^{-6} \ \text{m}^{-2}$ for MNCO and MCCO, respectively. These values provide information about the average oscillator strength and the characteristic wavelength of the optical transitions in the studied spinel ferrites. They are important parameters in understanding the optical behavior and electronic structure of materials. Comparing the values of S_0 and λ_0 for the MNCO and MCCO samples, we observe that both parameters are lower for MCCO. These differences indicate variations in the optical properties and behavior of the spinel chromites, potentially due to changes in their electronic structure or composition. On the

other hand, the static refractive index (n_0'') can be calculated as follows:[39]

$$n_0''^2 - 1 = \lambda_0^2 S_0 \tag{30}$$

The values for $n_0''^2$ were estimated, respectively, as 1.59 and 1.19 for the MNCO and MCCO, respectively. In particular, the estimated values of n_0'' agree well with those obtained from the Cauchy adjustment and the calculation from E_0 and E_d.

3.4.5. Non-linear optical parameters. Nonlinear optics delves into investigating the way light engages with matter. Typically, a material's optical reaction varies linearly in accordance with the magnitude of the electric field. Yet, under elevated power conditions, material properties may undergo swifter alterations, resulting in nonlinear phenomena. Linear and nonlinear susceptibilities are interconnected with induced polarization, manifested as a series of powers of the light's electric field intensity E, as governed by the following relation:[40]

$$P = \varepsilon_0[\chi^{(1)}E + \chi^{(2)}E^2 + \chi^{(3)}E^3 + \ldots] \tag{31}$$

where $\chi^{(1)}$ represents the linear susceptibility, and $\chi^{(2)}$ and $\chi^{(3)}$ denote the second and third-order nonlinear susceptibilities, respectively. However, Lines *et al.* have indicated that $\chi^{(2)}$ is nearly negligible in optically isotropic glasses and in crystals possessing a symmetry centre. The linear optical susceptibility ($\chi^{(1)}$) can be anticipated based on the linear refractive index as follows:

$$\chi^{(1)} = \frac{n^2 - 1}{4\pi} \tag{32}$$

The nonlinear optical susceptibility $\chi^{(3)}$ and the linear optical susceptibility $\chi^{(1)}$ are directly related according to Miller's rule:[41]

$$\chi^{(3)} = A \left[\frac{n^2 - 1}{4\pi}\right]^4 \cong A\left[\chi^{(1)}\right]^4 \tag{33}$$

where $A = 1.7 \times 10^{-10}$ esu is a frequency-independent constant,[40] with 1 esu being equivalent to 1.4×10^{-8} m^2 V^{-2}. In the extended wavelength range, as the product ($h\nu$) approaches zero, the refractive index tends to the static refractive index (n_0'), and eqn (32) and (33) become as follows:

$$\chi^{(1)} = \frac{n_0'^2 - 1}{4\pi} \tag{34}$$

$$\chi^{(3)} \cong A \left[\frac{E_d}{4\pi E_0}\right]^4 \tag{35}$$

The nonlinear refractive index n_2 can be expected from the nonlinear susceptibility $\chi^{(3)}$ *via* this relation:[41]

$$n_2 = \frac{12\pi\chi^{(3)}}{n_0'} \tag{36}$$

The anticipated values of $\chi^{(1)}$, $\chi^{(3)}$, and n_2 are also summarized in Table 4 for MNCO and MCCO samples. The values of

these parameters agree well with those found for other samples considered as promising candidates for nonlinear applications such as lasing, telecommunication, optical switching, modulators, optical information processing, and ultrafast optical communication.[40]

3.4.6. Optical conductivity and optical dielectric constants. In this section, we have evaluated the optical conductivity ($\sigma_{op}(\lambda)$), real component of optical permittivity ($\varepsilon_1(\lambda)$), imaginary component ($\varepsilon_2(\lambda)$), and optical loss factor ($\tan(\delta)$) for the MNCO and MCCO spinel chromites. The following equations were used to calculate these parameters based on the absorption coefficient (α), refractive index (n), speed of light (c), and extinction coefficient (k).[4,40]

$$\sigma_{opt} = \frac{\alpha(\lambda)n(\lambda)c}{4\pi k(\lambda)} \tag{37}$$

$$\varepsilon_1(\lambda) = n^2(\lambda) - k^2(\lambda) \tag{38}$$

$$\varepsilon_2(\lambda) = 2n(\lambda)k(\lambda) \tag{39}$$

$$\tan(\delta) = \frac{\varepsilon_2(\lambda)}{\varepsilon_1(\lambda)} \tag{40}$$

Based on the observed behavior of the optical conductivity ($\sigma_{op}(\lambda)$) as depicted in Fig. 7a, it is evident that the materials exhibit a strong photoresponse. The values of $\sigma_{op}(\lambda)$ were found to be higher at shorter wavelengths, indicating increased conductivity and light absorption in this range. Conversely, the values were weaker at longer wavelengths, suggesting reduced conductivity and absorption of light in that region. This behavior implies that the prepared materials are more responsive to light containing higher-energy photons. The higher conductivity at shorter wavelengths indicates a greater ability to conduct and interact with light in this energy range. This phenomenon could be attributed to the excitation of electrons within the material. As shown in Fig. 7b, the real part of the optical dielectric constant, $\varepsilon_1(\lambda)$, showed a similar trend to the refractive index, indicating a consistent behavior in the prepared chromites. This similarity suggests that changes in the refractive index can be attributed to variations in the $\varepsilon_1(\lambda)$ constant. Furthermore, the imaginary part of the dielectric constant, $\varepsilon_2(\lambda)$, shows a slight increase with increasing wavelength (see Fig. 7c). This indicates a minor level of absorption or energy dissipation as the wavelength becomes longer, making the samples suitable for efficient light absorption. This behavior is consistent with similar observations in other spinel compounds and can be attributed to various factors, such as electronic transitions, lattice vibrations, or defect-related processes within the material.[4,42] The optical loss factor, $\tan(\delta)$, quantifies the energy dissipation in the material when subjected to an electric or electromagnetic field. The behavior of $\tan(\delta)$ was examined in Fig. 7d, and it was found to increase with increasing wavelengths. This indicates an increase in energy dissipation or loss in the material as the wavelength becomes longer.[42]
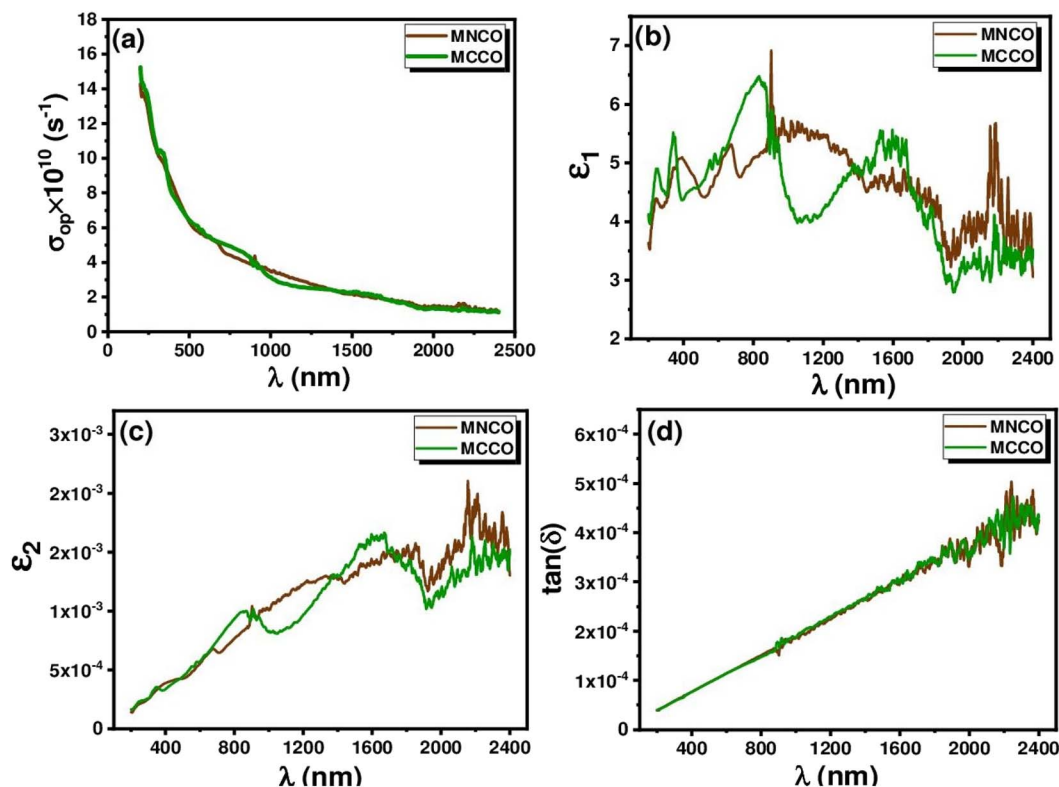
Fig. 7 (a) Optical conductivity (σ_{op}) *versus* λ for MNCO and MCCO spinel chromites. (b) Real part of dielectric permittivity $\varepsilon_1(\lambda)$. (c) Imaginary part of the dielectric permittivity $\varepsilon_2(\lambda)$. (d) Variation of the optical loss factor tan(δ).

4. Conclusion and future perspective

To conclude, the sol–gel-prepared $Mg_{0.6}Ni_{0.4}Cr_2O_4$ (MNCO) and $Mg_{0.6}Cu_{0.4}Cr_2O_4$ (MCCO) spinel chromites were confirmed to be pure single-phase samples based on X-ray diffraction analysis. The experimental structural parameters closely matched the theoretical values. FTIR spectroscopy was employed to investigate the elastic properties, revealing that MCCO exhibited lower elastic moduli and Debye temperature compared to MNCO. Furthermore, the band-gap (E_g) and Urbach (E_u) energies were also found to be lower for MCCO than MNCO. A comprehensive analysis of various optical parameters, including refractive index, penetration depth, extinction coefficients, nonlinear optical parameters, optical conductivity, and dielectric constants, was also presented. Our findings indicate that the substitution of Ni^{2+} and Cu^{2+} ions in magnesium chromites ($MgCr_2O_4$) enhances their visible light absorption. The MNCO and MCCO samples demonstrate significant advantages, including their easy and cost-effective synthesis, lower band-gap energies, good transparency, efficient light absorption, and effective energy conversion. These materials hold potential for various optoelectronic fields, including solar cells, photocatalysis, and nonlinear applications.

While our study has shed light on the promising characteristics of MNCO and MCCO spinel chromites, future research should focus on exploring a broader range of compositions to establish a comprehensive understanding of the structure–property relationships. Additionally, investigating the electrical conductivity and exploring doping strategies and surface modifications will be instrumental in enhancing the optoelectronic properties of these spinel chromites, enabling their integration into various technological applications.

Data availability

The data used to support the findings of this study are available from the corresponding author upon reasonable request.

Conflicts of interest

There are no conflicts to declare.

Acknowledgements

References

1 S. Ghotekar, S. Pansambal, V. H. Nguyen, S. Bangale, K. Y. A. Lin, H. C. A. Murthy and R. Oza, *J. Sol-Gel Sci. Technol.*, 2023, **105**, 176.
2 S. Ghotekar, D. Sanap, K. Y. A. Lin, H. Louis, D. Pore and R. Oza, *Res. Chem. Intermed.*, 2024, **50**, 49.

3 S. Ghotekar, D. Sanap, K. Patel, Y. Abhale, A. Chauhan, L. Li, D. Kumar, K. Y. A. Lin and R. Oza, *Res. Chem. Intermed.*, 2024, **50**, 2199.

4 M. L. Bouazizi, S. Hcini, K. Khirouni, F. Najar and A. H. Alshehri, *J. Inorg. Organomet. Polym.*, 2023, **33**, 2127.

5 Y. Benrighi, N. Nasrallah, T. Chaabane, H. Belkacemi, K. W. Bourkeb, H. Kenfoud and O. Baaloudj, *J. Sol-Gel Sci. Technol.*, 2022, **101**, 390.

6 S. P. Deshmukh, K. R. Sanadi, R. S. Diggikar, V. B. Koli and A. V. Mali, *J. Mater. Sci.: Mater. Electron.*, 2021, **32**, 6810.

7 L. Mao, H. Cui, C. Miao, H. An, J. Zhai and Q. Li, *J. Mater. Cycles Waste Manag.*, 2016, **18**, 573.

8 A. Abbasi, S. M. S. Sajadi, O. Amiri, M. Hamadanian, H. Moayedi, M. Salavati-Niasari and M. M. Beigi, *Composites, Part B*, 2019, **175**, 107077.

9 M. A. Kassem, A. A. El-Fadl, A. M. Nashaat and H. Nakamura, *J. Alloys Compd.*, 2019, **790**, 853.

10 V. Mykhailovych, A. Kanak, Ş. Cojocaru, E. D. C. Arsene, M. N. Palamaru, A. R. Iordan, O. Korovyanko, A. Diaconu, V. G. Ciobanu, G. Caruntu, O. Lushchak, P. Fochuk, Y. Khalavka and A. Rotaru, *Catalysts*, 2021, **11**, 1476.

11 A. Fujishima, X. Zhang and D. A. Tryk, *Surf. Sci. Rep.*, 2008, **63**, 515.

12 J. Xie, H. Wang, M. Duan and L. Zhang, *Appl. Surf. Sci.*, 2011, **257**, 6358.

13 N. R. Dhineshbabu, V. Rajendran, N. Nithyavathy and R. Vetumperumal, *Appl. Nanosci.*, 2016, **6**, 933.

14 D. P. Shoemaker and R. Seshadri, *Phys. Rev. B: Condens. Matter Mater. Phys.*, 2010, **82**, 214107.

15 K. Manjunatha, P. Z. Si, G. V. J. Gowda, A. El-Denglawey and V. J. Angadi, *Ceram. Int.*, 2022, **48**, 11654.

16 T. Tatarchuk, A. Shyichuk, I. Trawczyńska, I. Yaremiy, A. T. Pędziwiatr, P. Kurzydło, B. F. Bogacz and R. Gargula, *Ceram. Int.*, 2020, **46**, 27517.

17 R. D. Shannon, *Acta Crystallogr. Sect. A Cryst. Phys. Diffr. Theor. Gen. Crystallogr.*, 1976, **32**, 751.

18 M. A. Islam, A. K. M. A. Hossain, M. Z. Ahsan, M. A. A. Bally, M. S. Ullah, S. M. Hoque and F. A. Khan, *RSC Adv.*, 2022, **12**, 8502.

19 W. Zhang, A. Sun, X. Pan, Y. Han, X. Zhao, L. Yu, Z. Zuo and N. Suo, *J. Mater. Sci.: Mater. Electron.*, 2019, **30**, 18729.

20 T. Roisnel and J. Rodriguez-Carvajal, *LLB-LCSIM*, 2003.

21 M. A. Ahmed, S. F. Mansour and M. Afifi, *J. Magn. Magn. Mater.*, 2012, **324**, 4.

22 K. Pubby, K. V. Babu and S. B. Narang, *Mater. Sci. Eng. B.*, 2020, **255**, 114513.

23 K. B. Modi, *J. Mater. Sci.*, 2004, **39**, 2887.

24 Y. Gao, Z. Wang, J. Pei and H. Zhang, *J. Alloys Compd.*, 2019, **774**, 1233.

25 H. Dhibi, O. Rejaiba, J. Khelifi, M. Nasri, O. Amorri, K. Khirouni and M. L. Bouazizi, *J. Sol-Gel Sci. Technol.*, 2023, **108**, 159.

26 H. Dhibi, O. Rejaiba, J. Khelifi, M. Nasri, K. Khirouni, M. L. Bouazizi, E. K. Hlil and J. Inorg, *Organomet. Polym.*, 2023, **33**, 3984.

27 F. Hcini, S. Hcini, M. M. Almoneef, M. H. Dhaou, M. S. Alshammari, A. Mallah, S. Zemni, N. Lefi and M. L. Bouazizi, *J. Mol. Struct.*, 2021, **1243**, 130769.

28 F. Beshkar, S. Z. Ajabshir and M. S. Niasari, *J. Mater. Sci. Mater. Electron.*, 2015, **26**, 5043.

29 P. Choudhary and D. Varshney, *J. Magn. Magn. Mater.*, 2018, **454**, 274.

30 A. A. El-Fadl, A. M. Nashaat and M. A. Kassem, *Mater. Res. Express*, 2019, **6**, 1150a7.

31 M. Caglar, S. Ilican, Y. Caglar and F. Yakuphanoglu, *Appl. Surf. Sci.*, 2009, **255**, 4491.

32 S. R. Johnson and T. Tiedje, *J. Appl. Phys.*, 1995, **78**, 5609.

33 A. A. Ansari, M. Abushad, M. Arshad, S. Naseem, H. Ahmed, S. Husain and W. Khan, *J. Mater. Sci.: Mater. Electron.*, 2021, **32**, 21988.

34 S. Husain, A. O. A. Keelani and W. Khan, *Nano-Struct. Nano-Objects*, 2018, **15**, 17.

35 O. Rejaiba, K. Khirouni, M. H. Dhaou, B. Alzahrani, M. L. Bouazizi and J. Khelifi, *Opt. Quantum Electron.*, 2022, **54**, 315.

36 A. M. Alsaad, Q. M. Al-Bataineh, A. A. Ahmad, Z. Albataineh and A. Telfah, *Optik*, 2020, **211**, 164641.

37 S. H. Wemple and M. Didomenico, *Phys. Rev. B: Solid State*, 1971, **3**, 1338.

38 K. Tanaka, *Thin Solid Films*, 1980, **66**(3), 271.

39 A. M. Ismail, M. I. Mohammed and E. G. El-Metwally, *Indian J. Phys.*, 2019, **93**, 175.

40 F. Z. Rachid, L. H. Omari, H. Lassri, H. Lemziouka, S. Derkaoui, M. Haddad, T. Lamhasni and M. Sajieddine, *Opt. Mater.*, 2020, **109**, 110332.

41 V. Ganesh, L. Haritha, M. Anis, M. Shkir, I. S. Yahia, A. Singh and S. AlFaify, *Solid State Sci.*, 2018, **86**, 98.

42 W. Jdey, N. Hamdaoui, S. Hcini, S. Mansouri and L. El Mir, *Opt. Mater.*, 2024, **147**, 114666.